

Universal Quantum Simulation of 50 Qubits on Europe’s First Exascale Supercomputer Harnessing Its Heterogeneous CPU-GPU Architecture

Hans De Raedt^a, Jiri Kraus^b, Andreas Herten^a, Vrinda Mehta^{a,*}, Mathis Bode^a, Markus Hrywniak^b, Kristel Michielsen^a, Thomas Lippert^a

^a*Jülich Supercomputing Centre, Forschungszentrum Jülich, D-52425 Jülich, Germany*

^b*NVIDIA, Würselen, Germany*

Abstract

We have developed a new version of the high-performance Jülich universal quantum computer simulator (JUQCS-50) that leverages key features of the GH200 superchips as used in the JUPITER supercomputer, enabling simulations of a 50-qubit universal quantum computer for the first time. JUQCS-50 achieves this through three key innovations: (1) extending usable memory beyond GPU limits via high-bandwidth CPU-GPU interconnects and LPDDR5 memory; (2) adaptive data encoding to reduce memory footprint with acceptable trade-offs in precision and compute effort; and (3) an on-the-fly network traffic optimizer. These advances result in an 11.4-fold speedup over the previous 48-qubit record on the K computer.

Keywords: HPC simulation, quantum computing, GPU

1. Introduction

Quantum computing is rapidly advancing, promising breakthroughs in fields such as cryptography, materials science, quantum chemistry, and artificial intelligence [1]. However, due to the hardware limitations of contemporary quantum information processors, researchers rely heavily on simulators running on classical computers to bridge the gap between classical and quantum computing. In general, simulating quantum systems is a challenging task due to the exponential growth of computational requirements as the number of qubits increases [2].

Recent developments in high-performance quantum computer simulators have begun to address these challenges by exploiting advances in massively parallel computing architectures. In this context, JUQCS-50, a high-fidelity universal quantum computer simulator, demonstrates near-linear scalability of elapsed time with respect to the number of qubits, representing a significant improvement in the efficiency of large-scale quantum circuit simulations.

By leveraging the computational infrastructure of the JUNIQ (Jülich Unified Infrastructure for Quantum

Computing) platform, JUQCS-50 provides a robust environment for exploring quantum algorithms beyond the reach of current quantum hardware. This includes the simulation and benchmarking of key algorithms such as the Variational Quantum Eigensolver (VQE) and the Quantum Approximate Optimization Algorithm (QAOA) for systems of up to 50 qubits. Such capabilities enable accurate performance studies and algorithmic optimization, supporting the broader development of universal quantum computing methodologies.

In this work, we present a major milestone reached by JUQCS-50: the successful simulation of 50-qubit universal quantum computers for the first time. Utilizing the capabilities of the JUPITER supercomputer, the simulator runs efficiently on 16 384 GH200 superchips, using hybrid memory, adaptive byte encoding for mixed low-precision and FP64 arithmetic, and communication optimization to maximize memory usage and minimize network traffic. We show the technological advancements in JUQCS-50 and extensively study the performance on the supercomputer, including weak and strong scaling behaviour. By simulating both simple Hadamard gates and a more complex adder circuit, we are able to assess unique system and method features at the same time.

The remainder of this paper is organized as follows. The [next Section](#) briefly discusses the computational

*Corresponding author: v.mehta@fz-juelich.de

problem. [Section 3](#) provides an overview of the current state of the art in quantum computer simulation techniques. [Section 4](#) describes the methods and optimizations implemented in JUQCS-50 that enable simulations at the 50-qubit scale. [Section 5](#) introduces the performance metrics used to evaluate JUQCS-50, and [Section 6](#) presents the corresponding performance results. In [Section 7](#), we discuss an application of JUQCS-50 to adder circuits, including both the approach and results. Finally, [Section 8](#) concludes the paper with a summary of the key findings and perspectives for future work.

2. Problem statement

A universal quantum computer [2] simulator requires storage for the full state vector (wave function) describing the state of the quantum computer [2]. Using the FP64 representation, storing the (complex-valued) state vector for an N -qubit quantum computer requires 2^{N+4} bytes of memory, 2^4 accounting for the number of bytes required to store an element of the state vector. For example, representing the state of a $N = 32$ qubit quantum computer requires 64 GiB of memory in FP64 precision.

A quantum program is a sequence of quantum gates [2], each of which modifies the state vector. In general, each gate affects all the elements of the state vector. Simulating a single-qubit quantum gate amounts to multiplying all $2^{N/2}$ disjoint pairs of state-vector elements by a 2×2 matrix (corresponding to the quantum gate), the choice of pairs being determined by the particular qubit on which the quantum gate is applied. Similarly, simulating a two-qubit quantum gate amounts to multiplying all $2^{N/4}$ disjoint quadruples of state-vector elements by a 4×4 matrix (corresponding to the quantum gate), the choice of quadruples being determined by the particular qubits on which the gate is applied. As all these matrix-vector multiplications involve disjoint elements only, these operations can be carried out in parallel. Depending on the qubit(s) addressed, the pairs (quadruples) of vector elements may be located very far apart in memory. For instance, for a single-qubit gate acting on one of the qubits $k = 0, \dots, N-1$, the two indices of a pair differ by 2^k . This is a characteristic feature of a gate-based quantum computer simulator and is of prime importance when the state-vector becomes so large that the memory storing all its elements has to be distributed over several processing entities—NVIDIA Grace Hopper GH200 *superchips*, in our case (see [section 4](#)).

In the distributed-memory setting, it is convenient to use as the superchip index, the integer representation

of as many of the high-order bits of the element address as needed [3]. Let N' denote the number of qubits for which the state-vector fits into the memory of one GH200 superchip. Then the number of superchips n required to simulate an N qubit quantum computer and the number of state-vector elements L per superchip are given by $n = 2^{N-N'}$ and $L = 2^{N'}$, respectively. Performing a single-qubit gate on qubit with index $0 \leq j < N'$, requires no exchange of data between superchips because each pair of amplitudes that need to be updated resides in the memory of the same superchip, and all pairs can be updated in parallel. The same holds for two-qubit gates involving qubits $0 \leq j, k < N'$. These are the embarrassingly parallel cases: all superchips can perform the necessary calculations independently without any communication between the superchips. In contrast, for a single-qubit gate on qubit $N' \leq j < N$ (or a two-qubit gate with its target qubit [2] index exceeding $N' - 1$), superchips have to exchange data.

Focusing on the single-qubit case for simplicity, it follows that half of the state-vector elements stored in each superchip need to be exchanged [3]. This redistribution of elements always involves pairs of superchips, the indices of these superchips depending on the qubit that is being considered. For two-qubit gates, three-quarters of the number of elements need to be transferred between pairs of superchips.

As an example, consider simulating a $N = 40$ qubit quantum computer on the JUPITER supercomputer, requiring a total of $2 \times 8 \times 2^{40}/2^{30} = 16\,384$ GiB to store all state-vector elements in FP64 precision. Because of the inherent restriction to powers of two, characteristic of qubit systems, each GH200 GPU with 96 GiB memory (see [Figure 1](#) for a diagram of a node) can hold the equivalent of 2^{32} of these state-vector elements (64 GiB). This implies that with each single-qubit gate applied to a qubit with index $j > 31$, 16 384 GiB of data traverses through the network fabric before the gate operation can actually be carried out. Even for the fastest communication networks that are available today, it is clear that as the number of qubits N increases, the data exchange between superchips, when not performed efficiently, may become a very time-consuming and limiting part of the simulation. In summary,

1. Required memory and compute time increase exponentially with the number of qubits N .
2. The number of floating point operations per gate is given by $a2^N$, where a is a factor that depends weakly on the kind of gate.
3. For all gates involving qubits with indices smaller

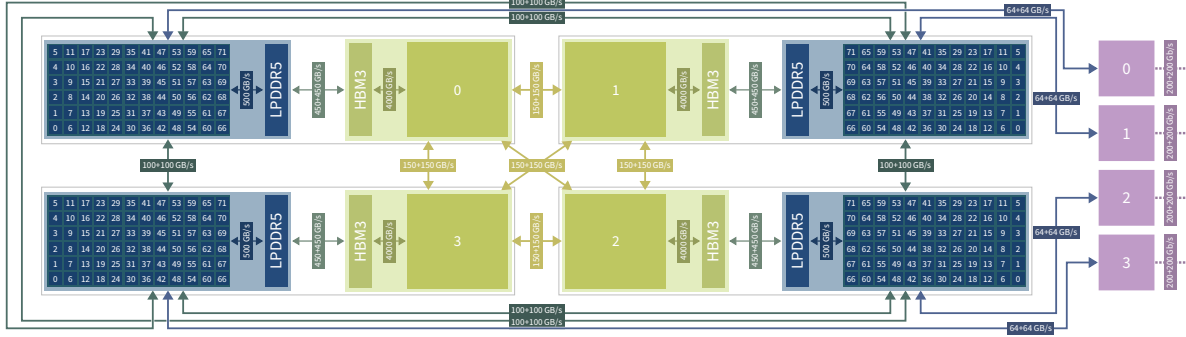


Figure 1: Overview of JUPITER’s quad GH200 node design with included technology and bandwidths. Each node contains four GH200 superchips, each comprising a tightly integrated CPU–GPU pair; see [section 4](#).

than N' , there is no communication between superchips.

4. For a single-qubit gate on the qubit with index $N' \leq j < N$, all superchips have to perform a send-receive operation, exchanging $2^{N'}/2$ elements of the state vector.
5. For a two-qubit gate involving a target qubit with index in the interval $[N', N]$, all pairs of superchips have to perform a send-receive operation, exchanging $3 \times 2^{N'}/4$ elements of the state vector

3. Current State of the Art

As explained above, dealing with the exponential growth of computational resources as the number of qubits increases is the main challenge of simulating quantum systems. Various techniques have been developed to address this challenge, each with its own strengths and weaknesses.

3.1. State Vector Simulation

Conceptually, state vector simulation is the most straightforward method, representing the full quantum state as a complex-valued vector of dimension 2^N , where N is the number of qubits.

This method allows for exact simulations but is resource-intensive. Examples are IBM Qiskit’s Aer-Simulator [4], Google Cirq [5], Eviden’s Qaptiva [6], and JUQCS [7, 8]. Memory and processing constraints currently limit the applicability of the three former examples to problems of 30–41 qubits. JUQCS goes significantly beyond this: the largest universal quantum computer JUQCS has simulated thus far contained 48 qubits [7].

Just like its predecessors [3, 7, 9], which have set multiple world records for simulating the largest universal quantum computers [10, 11], JUQCS-50 is designed with a strong emphasis on portability. It runs seamlessly across a wide spectrum of hardware platforms—from desktop PCs to high-end supercomputers with distributed and shared memory. This flexibility makes JUQCS-50 accessible to a broad user base, enabling both development and large-scale production runs in diverse computing environments. On CPU-based systems, only a Fortran 2003-compatible compiler (e.g., Intel IFX, gfortran, nvfortran) and standard MPI support are required. To utilize NVIDIA GPUs, JUQCS-50 additionally depends on CUDA-Fortran and CUDA-aware MPI, ensuring efficient execution while maintaining ease of deployment across systems. Notably, the majority of JUQCS-50 software development was conducted on the JUWELS Booster system [12], utilizing NVIDIA A100 GPUs and AMD CPUs. This preceded the operational launch of JUPITER and underscores the feasibility of enablement work on previous-generation hardware.

In general, to keep the elapsed time of universal quantum computer simulations within reasonable bounds, it is essential to have effective algorithms and hardware to handle the massive amount of data transfers that result from distributing memory over many computational units.

JUQCS-50 addresses all these issues, facilitating the simulation of 50 qubits on the imminent exascale computer JUPITER, deploying GH200 superchips. JUQCS-50 can exploit new powerful features of the superchips to enable the simulation of these qubits using 4096 JUPITER nodes, with a significant reduction of the elapsed time to execute quantum circuits.

3.2. Tensor Network Simulation

Tensor networks are mathematical structures that can efficiently represent quantum states if entanglement is limited. This approach can significantly reduce memory usage for circuits with low-depth or limited connectivity. Instead of storing the entire state vector, tensor network methods break down computations into small, manageable parts. In practice, they are very useful for simulating shallow circuits with limited entanglement and tree-like circuit structures. One prime, typical example of this approach is the random quantum circuit simulator for the new generation of Sunway Supercomputers [13]. This simulator exploits the particular structure of the random quantum circuits used in Google’s quantum supremacy work [14] to construct a very efficient scheme to compute a small fraction of the exponentially large number of amplitudes for systems containing up to 100 qubits [13]. In contrast, JUQCS was used to compare the frequencies of the states produced by the supremacy experiments with the exact simulation of several random quantum circuits employed in the experiments, up to $N = 43$ qubits [14].

3.3. Dedicated simulation software for Shor’s algorithm

Shor’s algorithm for factoring integers is one of the most anticipated applications of quantum computing [1, 2]. It also provides another instance of dedicated simulation software executing a particular quantum algorithm for problem sizes that are out of reach for universal quantum computer simulators. The largest semiprime that has been factored by a universal quantum computer simulator (JUQCS) executing Shor’s original algorithm is 65 531. This simulation required simulating a 48-qubit universal quantum computer [7]. In contrast, with a completely different, dedicated implementation of the same algorithm, employing GPUs and dedicated post-processing of the outcomes of the simulation [15], the largest semiprime that could be factored without exploiting prior knowledge of the solution is $549\,755\,813\,701 = 712\,321 \times 771\,781$ [15]. As in the case of tensor network simulation, this illustrates once more that comparing simulators, highly tuned to specific problems, with universal quantum computer simulators, is a delicate issue.

3.4. Summary

As a simulator of a universal quantum computer—capable of executing arbitrary quantum circuits composed of universal gates [2] (and beyond)—JUQCS distinguishes itself through unmatched performance and the ability to handle a record number of qubits.

For specific problems, such as low-depth random quantum circuits or Shor’s algorithm, certain alternative techniques, when combined with specific constraints on the questions being asked, can surpass JUQCS in terms of the number of qubits they can handle. However, these techniques lose their advantage when applied to universal quantum computation—assuming they could perform it at all.

4. Innovations Realized

Consider simulating an $N = 50$ qubit quantum computer in FP64 precision on a GH200-based system such as JUPITER. Storing all the elements of the state vector requires $2 \times 8 \times 2^N / 2^{40} = 2^{14} = 16\,384$ TiB of memory. In AI terminology, this quantum computer simulator can be viewed as a $2^{50} - 1 \approx 1024$ trillion (not billion) parameter model (-1 because of the normalization of the state vector).

JUPITER¹ has about 6000 nodes (24 000 superchips). The largest number of nodes that can actually be used for JUQCS is 4096 (16 384 superchips) due to the powers-of-two restriction. Each of the 16 384 superchips is equipped with 96 GiB of HBM3 (device) and 120 GiB of LPDDR5 (host) memory; 216 GiB in total per GH200 superchip. The memory available for storing the state vector elements is therefore $128\,\text{GiB}/\text{GH200} \times 16\,384\,\text{GH200s} = 2048\,\text{TiB}$, a factor of eight too small for simulating 50 qubits.

As previously demonstrated [7], the memory requirement can be reduced by a factor of eight by using a special form of adaptive byte encoding (see subsection 4.3), representing each state-vector element by 2 bytes ($2 \times 8\,\text{bit}$) instead of 16 bytes ($2 \times 64\,\text{bit}$, for a complex number in FP64 precision). This compression reduces precision in general cases (though not in specific ones, such as the gate sequences used for benchmarking in this work) and increases computation time (see subsection 4.3).

Employing this technique makes it possible to reach the 50-qubit barrier with a universal quantum computer simulator running on JUPITER. A key question, then, is how to let JUQCS-50 compute entirely on the GPU using also the LPDDR5 host memory in its GH200 superchip efficiently within the GPU-based execution with minimal performance impacts.

¹In this work, JUPITER refers to the Booster module of the JUPITER supercomputer. A CPU-centric second module, JUPITER Cluster, will be deployed in the future.

In conclusion, to push the boundaries of what can be simulated with state-of-the-art hardware such as JUPITER, it is necessary to

1. maximize the utilization of available memory across GH200 superchips (in powers of two)
2. minimize the elapsed time spent on communication

In the following, we outline our unique solutions for these requirements.

4.1. Intra-GH200 communication

The Grace Hopper superchip is a hardware-coherent GPU-accelerated system where all processors can access all memory with high performance through the 900 GB/s NVLink-C2C connection. The most productive approach to use the full memory is through the Unified Memory concept, in which applications interact with one large memory pool. The Operating System (*OS*; Linux) natively supports the GH200 superchip and views both the CPU and the GPU memory as separate NUMA (*Non-Uniform Memory Access*) nodes. It is thus possible to use native, OS-provided allocators and rely on the OS capabilities to utilize multiple NUMA nodes to create a single, large allocation exceeding the size of the memory of a single NUMA node, usable from both the CPU and GPU parts of GH200. Of course, the CUDA allocation mechanism can also be used. Approximately sorted with increasing programming effort, the options to use GH200's memories are:

- 1 Use `malloc()`, which does not require any code changes, and rely on OS and Unified Memory Driver heuristics for data placement.
- 2 Use `malloc()`, which does not require any code changes, and guide data placement externally with `numactl -interleave`².
- 3 Use `numa_alloc_onnode()` to explicitly place the real and the imaginary parts in different NUMA nodes.
- 4 Use Unified Memory Data Usage Hints of CUDA's Unified Memory API [16] to explicitly stripe allocations between LPDDR5 and HBM3 memory.

²Or `-weighted-interleave` which we could not use due to missing kernel support on the machines.

```

size_t bytes_remaining = size_in_bytes;
char* psi_r_pos = (char*)psi_r;
char* psi_i_pos = (char*)psi_i;
while (bytes_remaining >= current_chunk_size) {
    cudaMemAdvise_v2(psi_r_pos, current_chunk_size,
        ↳ cudaMemAdviseSetPreferredLocation,
        ↳ current_loc);
    cudaMemPrefetchAsync_v2(psi_r_pos,
        ↳ current_chunk_size, current_loc, 0, 0);
    cudaMemAdvise_v2(psi_i_pos, current_chunk_size,
        ↳ cudaMemAdviseSetPreferredLocation,
        ↳ current_loc);
    cudaMemPrefetchAsync_v2(psi_i_pos,
        ↳ current_chunk_size, current_loc, 0, 0);
    psi_r_pos += current_chunk_size;
    psi_i_pos += current_chunk_size;
    bytes_remaining -= current_chunk_size;
    std::swap(current_loc, next_loc);
    std::swap(current_chunk_size, next_chunk_size);
}

```

Listing 1: Core of the Unified Memory Data Usage Hints implementation.

- 5 Use explicit data movement functions from the CUDA API like `cudaMemcpyAsync()` to move portions of the data between host and device memories, combined with automatic, on-the-fly optimization of network traffic.

The Unified Memory Data Usage Hints support the Unified Memory Driver with indications of data locality and promise to be a good middle-ground between automated data placement and programming effort. The implementation uses code as outlined in Listing 1 to distribute page-size-aligned chunks alternately between the LPDDR5 and the HBM3 NUMA node iteratively. This mechanism balances concurrent HBM3 and LPDDR5 usage. In the code, `current_loc` is initialized with the HBM3 NUMA node of the GPU used by the process, while `next_loc` is initialized with the LPDDR5 NUMA node closest to that GPU. Through the two `chunk_size` variables, the ratio between HBM3 data and LPDDR5 data can be steered to maximize HBM usage, something that is not possible with plain `malloc()` and the `numactl -interleave` approach.

To evaluate the different possible approaches, we run a $N = 33$ qubit benchmark with Hadamard gates and 11 passes requiring 128 GB of memory on one GH200. Experiments with `malloc()` provided very poor performance³. Monitoring GPU memory usage indicated

³Conducted experiments have been canceled after exceeding a runtime of several minutes.

that this was because Unified Memory Driver migration heuristics caused frequent page migrations between LPDDR5 and HBM3 in the given memory oversubscription scenario. The same happened when combining `malloc()` with `numactl -interleave`, and also when using the Unified Memory Data Usage Hints to explicitly stripe. This unexpected effect is currently being investigated by the Unified Memory team at NVIDIA. We could work around the behavior by disabling access-counter-based memory migration, as described in the CUDA 12.4 release notes [17]. While using Data Usage Hints, we experimentally identified a 4/11 ratio of LPDDR5 to HBM3 data as the best-performing configuration. This closely approximates the theoretical optimum of $(128 - 96)/96 = 1/3$, while reserving sufficient space for auxiliary data structures.

Table 1: Comparison of memory over-subscription strategies on one GH200 superchip.

Strategy	Runtime (s)	Speedup (<i>rel</i>)
① <code>malloc()</code>	446.67	1
② <code>numactl</code>	160.00	2.8
③ <code>numa_malloc_onnode()</code>	101.57	4.4
④ Data Usage Hints	71.70	6.2
⑤ Explicit Data Copies	53.87	8.3

Already with additional NUMA-related knowledge as provided with `numactl`, significant performance improvements can be gained. The use of Data Usage Hints offers further gains with minimal programming effort and is particularly effective for applications with complex data patterns or in prototyping and exploratory scenarios.

The last, fifth option is to use explicit data movement functions to transfer data between HBM3 and LPDDR5 memory. A library of such explicit memory transfer functions is provided by the *Host State Vector Migration* feature of NVIDIA cuQuantum but details of the implementation or performance have not been published.

JUQCS-50 surpasses the basic use of explicit data movement functions by integrating asynchronous CUDA copy functions with a look-ahead analyzer of the input gate sequence, enabling the automated, dynamic optimization of data movements on-the-fly.

The performance of the five approaches is compared in Table 1 (access-counter-based memory migrations disabled). To enhance performance and ensure adaptability to applications requiring storage for multiple state vectors, we have opted to utilize explicit memory transfers and on-the-fly optimization of data move-

ments.

4.2. Inter-GH200 communication

We use standard CUDA-aware MPI library calls to exchange data between different GH200s and nodes and adopt the technique of Ref. [3], which minimizes the amount of data transfers automatically.

Exploiting the asynchronous stream feature provided by CUDA, packing and unpacking data during the send and receive operations of MPI reduces the time to perform the inter-GH200 communication by approximately 10 %.

In principle, the number of inter-GH200 data exchanges could be further reduced through independent preprocessing of the gate sequence, an approach external to JUQCS (see also section 7). As this represents a nontrivial challenge, it lies beyond the scope of the present work and is planned for future investigation.

Table 2: Specifications JUPITER Booster

Quantity	JUPITER Booster
Number of nodes	5884
Number of GH200	23 536
TDP per GH200	680 W
Total CPU LPDDR5 memory	2880 TB
Total GPU HBM3 memory	2304 TB
Interconnect Type	InfiniBand NDR200
Node Injection Bandwidth	4 × 200 Gbit/s
Network Topology	DragonFly+
Top500 Listing	Jun. 2025
Rmax	~1001 PFLOP/s
Rpeak	~1300 PFLOP/s

4.3. Byte-encoding of the state vector elements

In earlier work [7], we explored various ways to encode the complex values of the state vector with less than two double-precision numbers (2×64 bit). An adaptive encoding scheme that has been found to perform well is based on the polar representation of a complex number ($z = re^{i\theta}$) and uses an update strategy to adaptively and automatically tune the encoding/decoding scheme to the particular quantum circuit being executed. A key feature of the scheme is its capacity to retain algorithmic precision to FP64-levels for some simulations, like the ones presented in this work.

Obviously, using two (2×8 bit) instead of sixteen bytes (2×64 bit) to store each of the complex-valued elements of the state vector reduces the amount of memory by a factor of eight.

Of course, this memory reduction comes at the expense of additional compute time incurred by on-the-fly encoding and decoding during the execution of the gate. For instance, running the gate sequence for the $N = 32$ qubit case (which fits in the HBM3 memory of a single GH200) takes 5.74 s and 4.58 s of computation time in byte-encoded and FP64 modes, respectively. For $N > 33$ qubits, however, where inter-superchip data is transferred, the data transferred in FP64 mode is eight times greater than in byte-encoded mode.

In general, the amount of additional compute complexity depends on the gate and varies from very little in the case of the X or CNOT gate to a factor of two to three (depending on the hardware) for gates such as the Hadamard gate [7]. For the purpose of this work, the gate operations have been implemented as GPU device kernels.

5. Performance criteria

The quantum computer simulator used in this work, JUQCS-50, was already introduced above. The base program, JUQCS, looks back on a long history of performance-conscious evaluations [3, 7] and is used for a variety of scientific applications [7, 18]. To evaluate the computational efficiency of JUQCS-50, we consider several performance metrics that capture both user-level experience and system-level behavior.

The most relevant measure from the user’s perspective is the total elapsed time to simulate a quantum circuit. This walltime includes not only the gate operations themselves but also the initialization of data structures, MPI setup, I/O, and other runtime overheads.

Complementary metrics provide deeper insights into system performance, see [Appendix A](#). These include the pure computation time, MPI communication time, and the time spent transferring data between HBM3 and LPDDR5 memory within each GH200 superchip—along with the associated data volumes.

The NVIDIA Grace Hopper GH200 superchip is core to our work, combining a 72-core, ARM-based CPU (Grace) with a Hopper GPU in one package, connected through a unique 900 GB/s bus (NVLink-C2C, *Chip-to-Chip*). The platform offers cache coherency for all involved memories, even between different superchips. Together with the fast NVLink-C2C, this cache coherency enables our memory-oversubscribing method,

allowing access to the 120 GB LPDDR5 host memory and 96 GB HBM3 device memory from both processors with good performance. The involved bandwidths can be seen in the node diagram [Figure 1](#) with four GH200s.

JUPITER is built from NVIDIA GH200 superchips and provides four of these superchips per node. Since the available power is allocated per superchip, it must be shared between the Grace CPU and the Hopper GPU. Investigating how different power distribution strategies impact the overall performance is an important direction for future work. JUPITER employs an InfiniBand NDR fabric with a DragonFly+ topology with 25 groups and up to 240 nodes in a group, offering 4×200 Gbit/s injection bandwidth per node. An overview of some defining system parameters is given in [Table 2](#).

JUQCS-50 is implemented in modern Fortran and utilizes CUDA Fortran for GPU acceleration through the NVIDIA HPC SDK toolkit, version 25.5, and GPU-aware OpenMPI or ParaStationMPI on JUPITER. All results reported in this work have been obtained with the OpenMPI version.

As previously discussed, the memory required to simulate an N -qubit universal quantum computer grows exponentially with N . This exponential growth imposes a hard limit on the number of qubits that can be simulated, namely $N = 50$ on JUPITER. While the theoretical exponential scaling of computation time with N can be almost entirely mitigated through massive parallelization [3, 7], as discussed in the next section, memory—rather than elapsed time—becomes the primary limiting factor for most applications. As a result, weak-scaling performance, as a function of N , serves as the key indicator of performance. For completeness, we also present strong-scaling data for $N = 40$ qubits, where the number of GPUs increases from 4 to 128, with four GPUs per node.

6. Performance Results

In this section, we delve into the performance results obtained for JUQCS-50, focusing on the key metrics identified earlier. For clarity and completeness, detailed performance tables are provided in [Appendix A](#).

6.1. Quantum Circuit used for Benchmarking

To validate the results of byte-encoded simulations, it is expedient to use a gate sequence that does not suffer from precision loss due to this encoding. One such sequence consists of Hadamard gates [2] followed by the simultaneous measurement of the three components

of each qubit (which is only possible in simulation). Specifically, we use

$$\text{Circuit} = M H_1 H_{N-2} H_0 H_{N-1} H_{N-6} H_{N-5} \dots \\ \dots H_0 H_{N-5} \dots H_{N-1}, \quad (1)$$

where H_i denotes the Hadamard operation on qubit i and M represents the measurement of all qubits, see Figure 2 for a graphical representation. This sequence keeps a reasonable balance between computational workload and MPI-based communication overhead as N is varied. Note that the sequence Equation 1 is to be read from right to left.

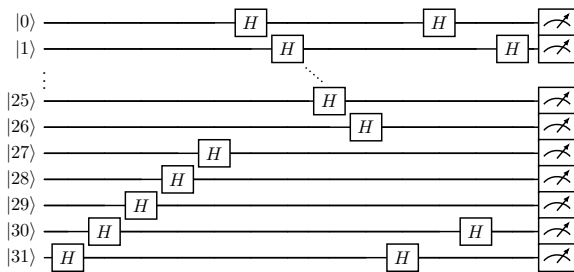


Figure 2: Graphical representation of the benchmark circuit Equation 1 for the case of $N = 32$ qubits. Operations proceed from left to right. Each application of a Hadamard gate (H) changes all the elements of the state vector. The rightmost symbol represents the simultaneous measurement of all three components of the Pauli-spin matrices representing a qubit, as performed by JUQCS-50. The initial state vector has all qubits in state zero.

6.2. Elapsed and Computation Times

Table A.5 lists the elapsed and compute times for JUQCS-50 executing a sequence of Hadamard gates on JUPITER in adaptive byte-encoded mode, using HBM3 and LPDDR5 memory, and on-the-fly optimization of data exchange, performing computation on the GPU only. In this mode, due to the intrinsic factor of two that is characteristic of quantum computers, the largest quantum computer that can be simulated on JUPITER (16 384 GH200 superchips) contains 50 qubits. In the case of a sequence of Hadamard gates followed by a measurement of all qubits, the use of the adaptive byte-encoding does not cause a loss of precision; that is, the final data are FP64-accurate by design, providing a non-trivial validation of the code.

Figure 3 presents the total elapsed time per gate operation, as well as the computation time per gate, across a range of qubit counts for two distinct sets of runs. The first set (labeled "1", data in Table A.5) was executed with JUQCS having exclusive access to the JUPITER

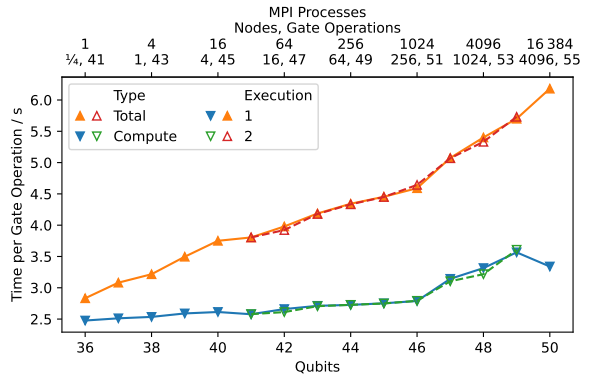


Figure 3: Total and compute elapsed times per gate operation for the range of qubits simulated on JUPITER (weak scaling). Lines are guides to the eye only.

supercomputer. In contrast, the second set (labeled "2") was executed on another day when other applications were concurrently running on JUPITER. One of the most striking conclusions is the apparent high reproducibility of the data.

Notably, the computation times remain nearly constant as the number of nodes (qubits) increases from 1 to 256 (36 to 46), while the total elapsed times reveal that the impact of network communication grows approximately linearly rather than exponentially with the number of qubits.

The computation time increases a little faster than theoretically expected. Based on the data in Table A.5, and taking the $N = 37$ case as a reference, we can estimate the expected computation time for the $N = 46$ case under ideal parallelism as $106\text{s} \times 51/42 = 129\text{s}$. This estimate is close to but still lower than the actual measured time of 142 s. The discrepancy arises from a combination of factors: interruptions in the byte decoding-encoding process due to global MPI communication (which is not accounted for in the reported MPI time), variability in GPU computation speeds, and network congestion. These factors become more important for $N > 46$, resulting in a notable change in the slopes of the lines through both the computation and elapsed times. At 47 qubits, executed on 512 nodes, the borders of one single DragonFly group with 240 nodes are safely surpassed, and a majority of communication happens through the tapered network between the groups, rather than inside them.

To examine the combined impact of global MPI communication, integral to the byte decoding–encoding process, variability in GPU computation speeds, and network congestion, as well as to showcase the versatil-

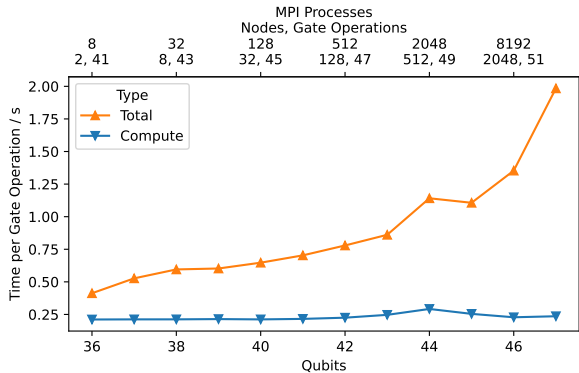


Figure 4: Total elapsed and compute times per gate operation for the range of qubits simulated on JUPITER in FP32 mode without using the LPDDR5 memory as an extension (weak scaling). When comparing to Figure 3, note the difference in scale of the y-axis and keep in mind that the number of GPUs used is eight times larger, see Table A.6. Lines are guides to the eye only.

ity of JUQCS-50, we conducted benchmarks in FP32 mode. In this configuration, state vector coefficients are stored in FP32 format, while all arithmetic operations are performed in FP64. Additionally, LPDDR5 was not used as a CPU memory extension. Figure 4 illustrates the computation time and total elapsed time per gate, with further details provided in Table A.6. The most striking observation is that, up to the maximum number of qubits supported by JUPITER in this mode, namely $N = 47$ and aside from a minor anomaly at $N = 44$, the computation time remains nearly constant. This indicates near-perfect weak scaling behavior across the qubit range from 36 to 47.

As expected, the total elapsed time increases with N , driven by the growing volume of data exchanged and compounded by network congestion, particularly since these benchmarks were executed concurrently with other users' workloads. This increase is noticeably faster than linear but still far slower than exponential.

We conclude that the change in slope observed for $N > 46$ in Figure 3 may be attributed to the increased computational burden of the byte decoding-encoding process, which demands substantially more arithmetic operations, intermittently disrupted by global MPI communication, the topology, and the fact that the FP32 benchmark did not use the LPDDR5 memory of the CPU as a memory extension.

Overall, the computation time demonstrates excellent weak scaling behavior. The impact of transmitting massive volumes of data across the network manifests as a relatively mild dependence on N in the weak scaling of the total elapsed time, a point that will be examined in

more detail later.

For the 36-qubit case, the elapsed times in Table A.5 and Table A.7 show that the FP64 version takes about 54 s to complete the task by using eight GH200 superchips, whereas the byte-encoded version accomplished the same task in about 116 s using only one GH200 superchip. Put differently, the byte-encoded version is about a factor of $8 \times 54 / (1 \times 116) \approx 3.7$ times more efficient.

Due to the communication making up a larger part of the elapsed time as the number of qubits increases, for the largest problem that can be run on JUPITER in FP64 mode, the gain in efficiency, due to using byte-encoding, is a factor $16384 \times 185 / (2048 \times 264) \approx 5.6$.

To put the performance of the GH200-based system in perspective: setting the earlier world record [7] for $N = 48$ qubits using byte-encoding took the K computer 3102 s and the TaihuLight system (without using accelerators) 8548 s. This amounts to a performance increase by a factor of $3102/286 = 10.8$ for the simulation of the same problem size on the JUPITER system over the K computer.

On the JUPITER supercomputer, the maximum number of qubits that can be simulated using JUQCS-50 varies by numerical precision and memory configuration. Specifically, in byte-encoded, FP32, and FP64 modes, the limits are 50 (49), 48 (47), and 47 (46) qubits, respectively, with and without LPDDR5 memory of the GH200. Using the largest FP64-simulatable problem (47 (46) qubits) as a reference, the corresponding benchmark execution times are 264 (101), 145 (103), and 185 (106) seconds for byte-encoded, FP32, and FP64 modes, respectively, utilizing 512 (512), 2048 (2048), and 4096 (4096) JUPITER nodes. These results demonstrate that for problems of large but not maximal size, JUQCS-50 enables optimization across numerical precision, runtime, and node count.

6.3. Network Performance

Regarding the data transfer rate between HBM3 and LPDDR5 memory in the same GH200 superchip, Tables A.5–A.8 show that this rate, which includes pre- and postprocessing of the buffers in GPU memory, is of the order of 100 GiB/s. The amount of data that is being exchanged within one GH200 superchip is (except for $N = 36$) more than a factor of two larger than the data that is being sent and received by the same superchip over the interconnects (column GPU-GPU MPI data). Because of the sequence-dependent pattern by which data is being sent over the network, a straightforward comparison of the transfer times is rather difficult.

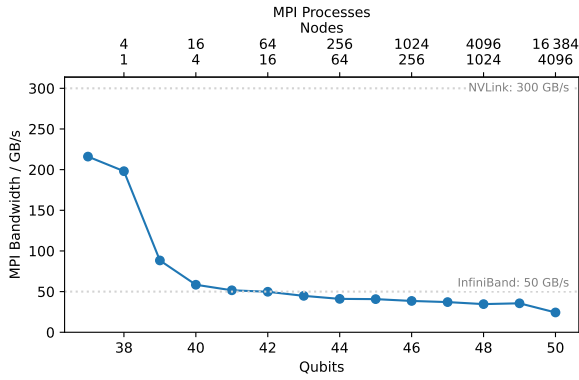


Figure 5: Measured communication bandwidth (in GiB/s) as a function of qubits (bottom) and MPI processes/nodes (top) with the expected performance shown for JUPITER. Horizontal lines indicate the limits of the interconnect bandwidths for comparison. The line through the data points is a guide to the eye only.

However, the data presented in Tables A.5–A.7 consistently show that the ratio of MPI communication time to GPU-CPU time increases as the number of qubits increases, even though the ratio of GPU-GPU MPI to GPU-CPU data decreases.

For $N = 50$ qubits, 2048 TiB of data is required to represent the state vector. With each single-qubit gate that requires MPI communication, half of this data travels through the network. In total, for the sequences used, there are 36 such network-active gate operations. The highly-optimized measurements of all the qubits require $13/14$ of all the data being exchanged. Thus, in total, for $N = 50$, $(36/2 + 13/14) \times 2048 \approx 38766$ TiB traverses the network in about 100 seconds, a respectable amount of TiB per second.

Disregarding small fluctuations, the MPI times listed in Table A.5 fit quite well to the function $5N - 180$ for $36 \leq N \leq 48$, the linear dependence reflecting the fact that $N - 33$ GPUs compete for network bandwidth to send and receive data. For $N \geq 43$, the linear N dependence shows up as a slowly decaying ($\approx \mathcal{O}(1/N)$) measured bandwidth depicted in Figure 5. Figure 5 also shows a sharp drop in bandwidth for $38 \leq N \leq 40$, signaling the transition from intra-node-dominated, fast NVLink communication (see Figure 1) to the slower, inter-node-dominated network-mode of communication.

6.4. Strong Scaling

Strong scaling has no real-world relevance from the viewpoint of quantum processing hardware because a quantum information processor having K qubits has no

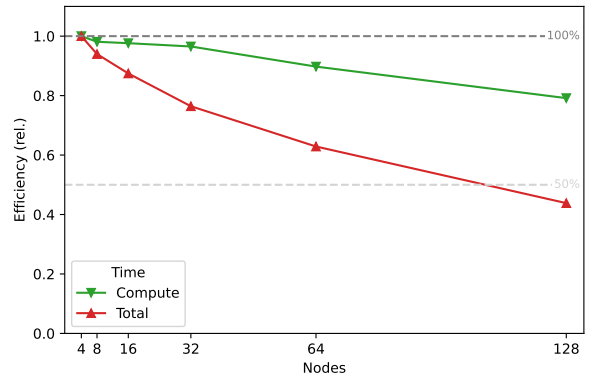


Figure 6: Relative efficiency measured (strong scaling) for 40 qubits over a range of MPI processes/nodes. Shown is the relative time with respect to the elapsed time on four nodes (16 MPI processes, $N = 40$ qubits). The lines through the data points are guides to the eye only.

way to distribute the execution over several units. However, from the viewpoint of benchmarking and simulation, it is interesting to study the strong scaling behavior of the algorithm and hardware. Table A.8 collects the data for fixed $N = 40$ and an increasing number of GPUs, always for the same quantum circuit, also see Figure 6.

The strong scaling data shows that the computation times and GPU-CPU communication times scale close to perfect, but, as expected, the total elapsed times do not, due to the necessary communication among nodes. As the number of MPI processes doubles, the GPUs have to exchange less data (by a factor of two) but they also have to compete with more GPUs (by a factor of two) for network bandwidth. From Table A.8, it follows that the measured time per GiB is 0.017, 0.020, 0.022, 0.027, 0.033 and 0.047 for 16, ..., 512 MPI processes, respectively. As the number of MPI processes increases, there is an initial, approximately linear increase of the time per GiB. Then, starting from 128 MPI processes, the time per GiB is dominated by the slower inter-node network and the measured time per GiB saturates at approximately 0.047 s/GiB or, equivalently, a bandwidth of 21 GiB/s, in rough agreement with the bandwidth (24 GiB/s, see Table A.8) for a large number of qubits. As there is the intrinsic limitation to powers of two, there is no way to determine accurately the number of MPI processes at which the saturation sets in.

6.5. Hopper GPU versus ARM CPU

Although not directly related to the use of the heterogeneous CPU-GPU architecture of the GH200 superchip, benchmarking the CPU and GPU components

separately is valuable from the standpoint of JUQCS-50 code portability. Table 3 presents data enabling such a comparison across the three precision modes currently supported by JUQCS-50. From this data we conclude that (i) storing the state vector in FP32 precision yields the fastest computation times for both CPU and GPU and (ii) MPI communication via the GPUs is faster than via the CPUs (which is to be expected from the design of the GH200 chip), and (iii) depending on the precision, the Hopper GPU accomplished the task a factor of ≈ 3 to 4 faster than the CPU. This is partially due to the fact that with JUQCS-50, the GPU computes faster than it can retrieve data from its HBM3 memory and, of course, this factor is also affected by the time used for MPI communication.

Table 3: Data obtained by running the benchmark circuit Equation 1 on either the Hopper GPU or the ARM CPU (using 64 of the 72 cores) of the GH200 superchip for $N = 40$ qubits and 256 MPI processes (64 nodes).

elapsed time (s)	computation time (s)	MPI time (s)	GPU-GPU MPI Data (GiB)	Compute engine	precision of state vector
16.14	7.24	6.08	111	GPU	BE
18.85	4.89	10.88	447	GPU	FP32
27.20	6.17	17.72	895	GPU	FP64
47.61	25.76	9.67	111	CPU	BE
40.49	14.29	23.72	447	CPU	FP32
119.42	63.96	52.43	895	CPU	FP64

6.6. Summary

Overall, Table A.5 and Figure 3 show that the elapsed time increases approximately linearly (not exponentially) with the number of qubits N . Recall that exponential scaling with the number of qubits N is a prime characteristic of universal quantum computing. Therefore, the fact that a simulator such as JUQCS-50 can simulate these computers in an elapsed time that grows approximately linearly with N is significant.

Our focus in this work was on optimizing the data movement, both on-superchip and beyond, to enable simulation of 50 qubits for a first time. Certainly, further fine-tuning potential exists for the novel GH200 platforms. In particular, the size of the buffers and the number of streams used for communication are unlikely to be optimal yet, and GPU device kernels that perform recursion can also be improved.

7. Application: Adder Circuits

Sequences of Hadamard gates are well-suited for benchmarking purposes because: (i) they are simple

to implement and yield known outcomes, (ii) their execution time is typically under 10 minutes, (iii) they exert significant stress on the communication network, and (iv) they maintain full precision without loss due to byte-encoding, which simplifies validation.

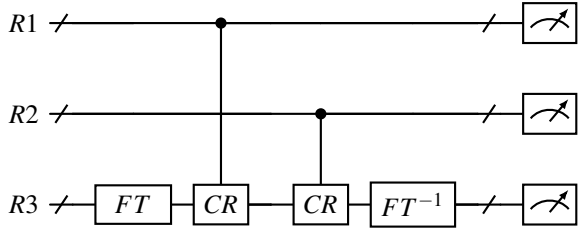


Figure 7: Structure of quantum circuit to add three M bit integers encoded in quantum registers $R1$, $R2$, $R3$ consisting of M qubits. The sum of the integers is returned in register $R3$, the qubits of other registers being untouched. By construction, integer addition is modulo M . FT: quantum circuit to perform a discrete Fourier transform [2]; CR: collection of controlled phase shifts. The right most symbol represents the simultaneous measurement of all three components of the Pauli-spin matrices representing a qubit, as performed by JUQCS-50. The structure trivially generalizes to fewer and more registers encoding integers.

Quantum algorithms that perform integer addition using quantum registers represent another valuable class of quantum circuits. (i) They are nontrivial in that they incorporate quantum Fourier transforms and controlled phase shifts, both core components of foundational quantum algorithms such as phase estimation [2] and Shor’s algorithm [15, 19]. (ii) The final output of the quantum computation, being the sum of the input integers, is easily validated. (iii) These circuits can place a substantial load on the communication network, offering a rigorous test of system performance. (iv) When executed in byte-encoding mode, due to the presence of controlled phase shifts, they may suffer a loss of numerical precision, providing information about the effect of using byte-encoding on the accuracy of the quantum computation.

A bird’s-eye view of a quantum circuit to add (superpositions of) three integers stored in the registers $R1$, $R2$, and $R3$, is shown in Figure 7. Each of these registers is assumed to consist of M qubits, enabling representing integers in the range $[0, 2^M - 1]$. Following Draper [20], the idea is to perform a (quantum) Fourier transform (FT) on $R3$, then apply the controlled phase shifts (CU) to accumulate the information stored in $R1$ and $R2$ in to the phases of the coefficients of the (partial) state vector in $R3$, and finally perform an inverse (quantum) Fourier

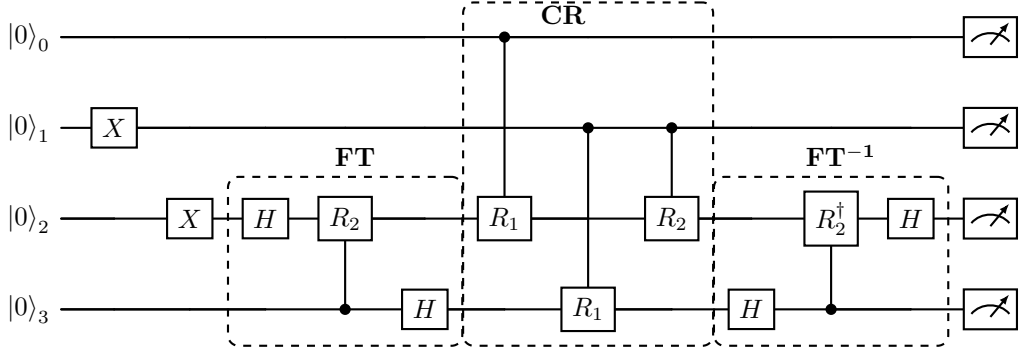


Figure 8: Realization of the quantum adder circuit shown in Fig. 7 for the case of two two-bit integers ($M = 2$). The first two gates (denoted by X) are not part of the adder circuit but serve to encode the integers 1 and 2 in registers $R1$ and $R2$, respectively (see text). X : interchanges qubit state 0 and 1; H : Hadamard gate; R_k : controlled phase shift by $2\pi/2^k$. See Ref. [2] for a detailed description of these gates.

transform (FT^{-1}) to transfer the information contained in the phases back to integer representation. The diagram in Figure 7 illustrates the structure of a circuit that adds (superpositions of) integers stored in three registers. However, the design generalizes straightforwardly to any number of registers.

As an illustration, Figure 8 presents the quantum circuit for adding two integers each one represented by a two-qubit register ($M = 2$). The X gates flip the states of qubits 1 and 2 from $|0\rangle_1$ and $|0\rangle_2$ to $|1\rangle_1$ and $|1\rangle_2$, respectively. Due to the structure of the FT used [2], the most significant bit of the integer is stored in the least significant bit of the register. Therefore, after performing the X gates, the state in $R1$ encodes the integer 1 and the state in $R2$ encodes the integer 2. Upon measurement, the state yields $\{0, 1, 1, 1\}$, the last two bits encoding $1 + 2 = 3$.

As an illustration and also to scrutinize the effect of using byte-encoding on the final result of a quantum computation, we use JUQCS-50 to execute a quantum circuit for adding two 25-bit integers ($M = 25$) with $R1$ encoding 21346502 and $R2$ encoding 12207929. The quantum circuit contains 1001 gates, which is too large to be displayed graphically on one page. The integers have been chosen so that their binary sum (being $2^{25} - 1$) results in a sequence of all ones. Translated into qubit language, this implies that all the expectation values of the z -components of the qubits ($\langle Q_z(i) \rangle$) are equal to one, allowing the correctness of the output to be visually confirmed at a glance.

Table 4 shows the results of the simulation. It is immediately clear that the quantum circuit yields the correct values of $\langle Q_z(i) \rangle$. Also clear is that due to the use of byte encoding, some expectation values of the x - and y -components deviate from the exact result $1/2$.

It is worth noting that, unless proven otherwise, cur-

rent quantum devices are unlikely to perform integer addition with the level of precision achieved by JUQCS-50 in its byte-encoded mode [21].

The quantum adder circuit also provides a nice example to explore how much can be gained by optimizing the circuit with respect to the amount of MPI communication. In its generic form shown in Figure 7, it took JUPITER 1996 s (180 s MPI GPU-GPU time, 720 s GPU-CPU time) to execute the quantum circuit. Simply interchanging the roles of $R1$ and $R2$ by relabeling the qubits (an operation that is part of JUQCS-50's instruction repertoire), reduces this time to 1193 s (69 s MPI GPU-GPU time, 335 s GPU-CPU time). This substantial performance improvement is solely attributed to the reduction in communication.

More broadly, it is evident that strategically relabeling qubits to minimize inter-GPU communication can significantly decrease the total execution time of simulating a quantum circuit. Optimizing the quantum circuit in this regard can be performed independently of JUQCS-50 and is therefore beyond the scope of the present study, but important future research.

8. Summary

JUQCS-50 efficiently utilizes the available hardware, CPUs, GPUs, and a combination of both, by exploiting the architectural strengths of modern systems like the GH200 superchips. It makes full use of memory resources (always in powers of two), extending beyond the GPU limits by leveraging the high-bandwidth CPU-GPU interconnect and LPDDR5 host memory. Its adaptive data encoding scheme reduces memory requirements at the cost of increased computation, while a built-in, on-the-fly optimizer minimizes network traffic. These innovations not only enable the aforemen-

Table 4: JUQCS-50 results for a 50-qubit quantum circuit designed to add two 25-bit integers (see text). Only the 25 expectation values of the qubits in register $R2$ are shown (qubits are numbered starting from zero).

Qubit	$\langle Q_x(i) \rangle$	$\langle Q_y(i) \rangle$	$\langle Q_z(i) \rangle$
24	0.50	0.50	1.00
25	0.50	0.52	1.00
26	0.51	0.50	1.00
27	0.50	0.50	1.00
28	0.50	0.50	1.00
29	0.50	0.50	1.00
30	0.50	0.50	1.00
31	0.50	0.50	1.00
32	0.50	0.50	1.00
33	0.50	0.50	1.00
34	0.50	0.50	1.00
35	0.50	0.50	1.00
36	0.50	0.50	1.00
37	0.50	0.50	1.00
38	0.50	0.50	1.00
39	0.50	0.50	1.00
40	0.50	0.50	1.00
41	0.50	0.50	1.00
42	0.50	0.50	1.00
43	0.50	0.50	1.00
44	0.50	0.50	1.00
45	0.50	0.50	1.00
46	0.50	0.50	1.00
47	0.48	0.49	1.00
48	0.50	0.50	1.00
49	0.50	0.50	1.00

tioned large-scale realistic simulations of user-defined circuits but, at the same time, combined with its ease of deployment and operation, JUQCS-50 can continuously and controllably stress both computational units and the network over defined periods, making it an ideal and realistic benchmark user application.

From the data presented in Tables A.5–A.7, it follows that, to a good approximation, the elapsed time increases approximately linearly with the number of qubits N , rather than exponentially. In other words, when combined with massively parallel computers, the universal quantum computer simulator JUQCS-50 overcomes the exponential scaling characteristic of gate-based quantum computers.

The advanced JUQCS-50, the newly developed version of JUQCS, will empower researchers to 1) perform exact simulations of arbitrary quantum circuits with varying degrees of accuracy, still far better than offered by current, state-of-the-art quantum computing hardware; 2) study the effects of noise and errors on quantum algorithms; 3) perform simulations of quantum annealing and quantum spin-dynamics for a wide vari-

ety of model Hamiltonians over a time span and with an accuracy that is not within reach of state-of-the-art quantum computing hardware; 4) expand simulations to larger quantum systems while keeping simulation times low; 5) benchmark (super)computers [3, 7, 18, 22].

JUQCS-50 is currently being integrated into JUNIQ [23], the Jülich UNified Infrastructure for Quantum Computing, providing science and industry access to state-of-the-art quantum computing emulators and devices. With JUPITER operational, JUQCS-50 will enable the study of problems up to 500 to 1000 times larger than those currently handled by other simulators (as discussed in section 3), thereby unlocking a new range of universal quantum computing applications yet to be explored. More specifically, JUQCS-50 will allow researchers to run applications such as variational quantum eigensolvers (VQE) [24–26], quantum approximate optimization algorithms (QAOA) [7, 8, 27–29], and quantum annealing [30] with an accuracy that is beyond the reach of state-of-the-art quantum computer hardware for systems with up to 50 qubits.

Acknowledgments

We acknowledge support from the following entities: The Ministry of Culture and Science of the State of North Rhine-Westphalia (MKW-NRW) for the project EPIQ; MKW-NRW together with EuroHPC JU, the German Federal Ministry of Education and Research (BMBF) for the project JUNIQ. This project received access to the JUPITER supercomputer, which is funded by the EuroHPC Joint Undertaking, the German Federal Ministry of Research, Technology and Space, and the Ministry of Culture and Science of the German state of North Rhine-Westphalia, through the JUPITER Research and Early Access Program (JUREAP). We thank the Swiss National Supercomputing Center CSCS for providing access to the Alps supercomputer, which was essential to prepare our workload for JUPITER.

References

- [1] S. S. Gill, S. Tuli, M. Xu, I. C. Singh, S. Duttar, R. Buyya, Quantum computing: A taxonomy, systematic review and future directions, *Software: Practice and Experience* 52 (2022) 92–136. doi:[10.1002/spe.2958](https://doi.org/10.1002/spe.2958).
- [2] M. Nielsen, I. Chuang, *Quantum Computation and Quantum Information*, 10th anniversary edition ed., Cambridge University Press, Cambridge, 2010. doi:[10.1017/cbo9780511976667](https://doi.org/10.1017/cbo9780511976667).

[3] K. De Raedt, K. Michielsen, H. De Raedt, B. Trieu, G. Arnold, M. Richter, Th. Lippert, H. Watanabe, N. Ito, Massively parallel quantum computer simulator, *Comp. Phys. Comm.* 176 (2007) 121 – 136. doi:[10.1016/j.cpc.2006.08.007](https://doi.org/10.1016/j.cpc.2006.08.007).

[4] The Qiskit Community, Qiskit: An open-source framework for quantum computing, 2023. URL: <https://qiskit.org/>.

[5] The Cirq Developers, Cirq: A python framework for nisq-era quantum circuits, 2023. URL: <https://quantumai.google/cirq>.

[6] Eviden, Qaptiva: Quantum application development platform, 2023. URL: <https://eviden.com/solutions/advanced-computing/quantum-computing/qaptiva-hpc/>.

[7] H. De Raedt, F. Jin, D. Willsch, M. Willsch, N. Yoshioka, N. Ito, S. Yuan, K. Michielsen, Massively parallel quantum computer simulator, eleven years later, *Comp. Phys. Comm.* 237 (2019) 47 – 61. doi:[10.1016/j.cpc.2018.1.1005](https://doi.org/10.1016/j.cpc.2018.1.1005).

[8] M. Willsch, D. Willsch, F. Jin, H. De Raedt, K. Michielsen, Benchmarking the quantum approximate optimization algorithm, *Quantum Information Processing* 19 (2020). doi:[10.1007/s1128-020-02692-8](https://doi.org/10.1007/s1128-020-02692-8).

[9] D. Willsch, M. Willsch, F. Jin, K. Michielsen, H. De Raedt, GPU-accelerated simulations of quantum annealing and the quantum approximate optimization algorithm, *Comp. Phys. Comm.* 278 (2022) 108411. doi:[10.1016/j.cpc.2022.108411](https://doi.org/10.1016/j.cpc.2022.108411).

[10] HPCwire, Quantum computer simulation: New world record on jugene, 2010. URL: https://www.hpcwire.com/2010/06/28/quantum_computer_simulation_new_world_record_on_jugene/.

[11] HPCwire, World record: Quantum computer with 46 qubits simulated, 2017. URL: <https://www.hpcwire.com/2017/12/18/world-record-quantum-computer-46-qubits-simulated/>.

[12] D. Alvarez, JUWELS cluster and booster: Exascale pathfinder with modular supercomputing architecture at Jülich Supercomputing Centre, *Journal of large-scale research facilities JLSRF* 7 (2021). doi:[10.17815/jlsrf-7-183](https://doi.org/10.17815/jlsrf-7-183).

[13] Y. Liu, X. Liu, F. Li, H. Fu, Y. Yang, J. Song, P. Zhao, Z. Wang, D. Peng, H. Chen, C. Guo, H. Huang, W. Wu, D. Chen, Closing the “quantum supremacy” gap: achieving real-time simulation of a random quantum circuit using a new Sunway supercomputer, in: *Proceedings of the International Conference for High Performance Computing, Networking, Storage and Analysis, SC ’21*, ACM, 2021. doi:[10.1145/3458817.3487399](https://doi.org/10.1145/3458817.3487399).

[14] Google AI Quantum, collaborators, Quantum supremacy using a programmable superconducting processor, *Nature* 574 (2019) 505–510. doi:[10.1038/s41586-019-1666-5](https://doi.org/10.1038/s41586-019-1666-5).

[15] D. Willsch, M. Willsch, F. Jin, H. De Raedt, K. Michielsen, Large-scale simulation of Shor’s quantum factoring algorithm, *Mathematics* 11 (2023) 4222. doi:[10.3390/math11194222](https://doi.org/10.3390/math11194222).

[16] Cuda c++ programming guide - data usage hints section, Last retrieved on April 1, 2025. URL: <https://docs.nvidia.com/cuda/cuda-c-programming-guide/index.html#data-usage-hints>.

[17] Cuda 12.4 release notes - general cuda section, Last retrieved on April 1, 2025. URL: <https://docs.nvidia.com/cuda/archive/12.4.0/cuda-toolkit-release-notes/index.html#general-cuda>.

[18] D. Willsch, H. Lagemann, M. Willsch, F. Jin, H. De Raedt, K. Michielsen, Benchmarking supercomputers with the Jülich Universal Quantum Computer Simulator (2019). doi:[10.48550/ARXIV.1912.03243](https://doi.org/10.48550/ARXIV.1912.03243).

[19] P. Shor, Polynomial-time algorithms for prime factorization and discrete logarithms on a quantum computer, *SIAM Review* 41 (1999) 303.

[20] T. G. Draper, Addition on a quantum computer, *arXiv:quant-ph/0008033* (2000).

[21] K. Michielsen, M. Nocon, D. Willsch, F. Jin, Th. Lippert, H. De Raedt, Benchmarking gate-based quantum computers, *Comp. Phys. Comm.* 220 (2017) 44 – 55.

[22] A. Herten, S. Achilles, D. Alvarez, J. Badwaik, E. Behle, M. Bode, T. Breuer, D. Caviedes-Voullième, M. Cherti, A. Dabah, S. E. Sayed, W. Frings, A. Gonzalez-Nicolas, E. B. Gregory, K. H. Mood, T. Hater, J. Jitsev, C. M. John,

J. H. Meinke, C. I. Meyer, P. Mezentsev, J.-O. Mirus, S. Nassyr, C. Penke, M. Römmер, U. Sinha, B. v. S. Vieth, O. Stein, E. Suarez, D. Willsch, I. Zhukov, Application-Driven Exascale: The JUPITER Benchmark Suite, in: SC24: International Conference for High Performance Computing, Networking, Storage and Analysis, IEEE, 2024, pp. 1–45. doi:[10.1109/sc41406.2024.00038](https://doi.org/10.1109/sc41406.2024.00038).

[23] JUNIQ: The Jülich UNified Infrastructure for Quantum Computing, Last retrieved on April 1, 2025. URL: <https://www.fz-juelich.de/en/ias/jsc/systems/quantum-computing/juniq-facility/juniq>.

[24] A. Peruzzo, J. McClean, P. Shadbolt, M.-H. Yung, X.-Q. Zhou, P. J. Love, A. Aspuru-Guzik, J. L. O’Brien, A variational eigenvalue solver on a quantum processor, *Nature Communications* 5 (2014) 4213. doi:[10.1038/ncomms5213](https://doi.org/10.1038/ncomms5213).

[25] J. R. McClean, J. Romero, R. Babbush, A. Aspuru-Guzik, The theory of variational hybrid quantum-classical algorithms, *New Journal of Physics* 18 (2016) 023023. doi:[10.1088/1367-2630/18/2/023023](https://doi.org/10.1088/1367-2630/18/2/023023).

[26] M. Cerezo, A. Arrasmith, R. Babbush, S. Benjamin, S. Endo, K. Fujii, J. McClean, K. Mitarai, X. Yuan, L. Cincio, P. Coles, Variational quantum algorithms, *Nature Reviews Physics* 3 (2021) 625–644. doi:[10.1038/s42254-021-00348-9](https://doi.org/10.1038/s42254-021-00348-9).

[27] E. Farhi, J. Goldstone, S. Gutmann, A quantum approximate optimization algorithm, arXiv preprint arXiv:1411.4028 (2014). URL: <https://arxiv.org/abs/1411.4028>.

[28] L. Zhou, S.-T. Wang, S. Choi, H. Pichler, M. D. Lukin, Quantum approximate optimization algorithm: Performance, mechanism, and implementation on near-term devices, *Phys. Rev. X* 10 (2020) 021067. URL: <https://link.aps.org/doi/10.1103/PhysRevX.10.021067>. doi:[10.1103/PhysRevX.10.021067](https://doi.org/10.1103/PhysRevX.10.021067).

[29] P. C. Lotshaw, T. Nguyen, A. Santana, et al., Scaling quantum approximate optimization on near-term hardware, *Sci. Rep.* 12 (2022). URL: <https://doi.org/10.1038/s41598-022-14767-w>. doi:[10.1038/s41598-022-14767-w](https://doi.org/10.1038/s41598-022-14767-w).

[30] K. Vyas, F. Jin, H. De Raedt, K. Michielsen, Quantum speed-up for solving the one-dimensional Hubbard model using quantum annealing, arXiv:quant-ph/2510.02141 (2025).

Appendix A. Raw performance data

Table A.5: Elapsed and compute times for executing Hadamard gates [2] in a sequence designed to challenge both computation and communication on JUPITER, with JUQCS-50 employing adaptive byte-encoding, using both HBM3 and LPDDR5 memory and on-the-fly optimization of data exchange (weak scaling). The column GPU-GPU MPI lists the data send and received by each of the GPUs (using CUDA-aware MPI). MPI time includes the time encoding and decoding buffers for transmitting these data. The columns 'GPU-CPU data' and 'count' specify the volume of data and the number of data exchanges between HBM3 and LPDDR5 memory. GPU-CPU time includes the time for writing and reading buffers in HBM3 memory. The column #gate operations is the number of Hadamard operations plus the measurement of each of the qubits. The simulation of a 50-qubit, universal quantum computer on JUPITER sets a new world record.

Qubits	memory (GiB)	MPI processes	elapsed time (s)	computation time (s)	#gate operations	MPI time (s)	GPU-GPU MPI Data (GiB)	GPU-CPU time (s)	GPU-CPU Data (GiB)	GPU-CPU count
36	1026	1	116.13	101.54	41	0.00	0	11.60	1216	19
37	2052	2	129.43	105.51	42	2.37	512	17.99	2048	32
38	4104	4	138.31	108.99	43	4.20	832	20.23	2368	37
39	8208	8	153.83	113.96	44	12.68	1120	22.46	2688	42
40	16416	16	168.77	117.59	45	21.63	1264	24.54	2944	46
41	32832	32	175.00	118.55	46	24.64	1272	26.43	3136	49
42	65664	64	187.04	125.00	47	28.19	1404	28.51	3392	53
43	131328	128	200.97	130.16	48	34.25	1534	30.59	3648	57
44	262656	256	212.78	133.61	49	40.50	1663	32.64	3904	61
45	525312	512	222.71	137.59	50	43.94	1791	34.77	4160	65
46	1050624	1024	234.13	142.25	51	49.82	1919	36.81	4416	69
47	2101248	2048	263.86	163.43	52	55.15	2047	38.88	4672	73
48	4202496	4096	286.27	175.67	53	62.81	2175	40.94	4928	77
49	8404992	8192	307.83	192.56	54	64.65	2303	43.00	5184	81
50	16809984	16384	339.96	183.69	55	99.81	2431	45.08	5440	85

Table A.6: Same as Table A.5 except that all calculations were performed with JUQCS-50 running in FP32 mode and without using the LPDDR5 memory as an extension (weak scaling).

Qubits	memory (GiB)	MPI processes	elapsed time (s)	computation time (s)	#gate operations	MPI time (s)	GPU-GPU MPI Data (GiB)	GPU-CPU time (s)	GPU-CPU Data (GiB)	GPU-CPU count
36	1040	8	16.92	8.66	41	6.26	560	0.00	0	0
37	2080	16	22.13	8.91	42	10.88	632	0.00	0	0
38	4160	32	25.60	9.13	43	13.74	700	0.00	0	0
39	8320	64	26.51	9.43	44	14.29	766	0.00	0	0
40	16640	128	29.12	9.54	45	16.33	831	0.00	0	0
41	33280	256	32.35	9.93	46	19.14	895	0.00	0	0
42	66560	512	36.62	10.58	47	22.38	959	0.00	0	0
43	133120	1024	41.33	11.85	48	26.90	1023	0.00	0	0
44	266240	2048	55.92	14.31	49	37.87	1087	0.00	0	0
45	532480	4096	55.33	12.72	50	38.03	1151	0.00	0	0
46	1064960	8192	69.02	11.64	51	50.69	1215	0.00	0	0
47	2129920	16384	103.19	12.28	52	78.34	1279	0.00	0	0

Table A.7: Same as Table A.5 except that all calculations were performed with JUQCS-50 running in FP64 mode (weak scaling).

Qubits	memory (GiB)	MPI processes	elapsed time (s)	computation time (s)	#gate operations	MPI time (s)	GPU-GPU MPI Data (GiB)	GPU-CPU time (s)	GPU-CPU Data (GiB)	GPU-CPU count
36	1040	8	53.75	11.06	41	12.11	1120	25.24	2560	40
37	2080	16	65.17	12.60	42	22.12	1264	24.45	2816	44
38	4160	32	63.98	11.47	43	24.00	1272	23.04	3008	47
39	8320	64	70.22	12.10	44	27.65	1404	24.97	3264	51
40	16640	128	82.74	15.69	45	32.89	1534	27.47	3520	55
41	33280	256	82.71	12.81	46	35.04	1663	28.78	3776	59
42	66560	512	87.52	13.16	47	37.42	1791	30.65	4032	63
43	133120	1024	98.06	13.86	48	46.24	1919	32.54	4288	67
44	266240	2048	109.98	13.56	49	55.18	2047	34.46	4544	71
45	532480	4096	124.06	16.24	50	59.02	2175	36.36	4800	75
46	1064960	8192	150.05	18.61	51	65.45	2303	38.25	5056	79
47	2129920	16384	185.19	32.99	52	91.09	2431	40.18	5312	83

Table A.8: Same as Table A.5 except that all calculations were performed for the same number of qubits $N = 40$ (strong scaling).

Qubits	memory (GiB)	MPI processes	elapsed time (s)	computation time (s)	#gate operations	MPI time (s)	GPU-GPU MPI Data (GiB)	GPU-CPU time (s)	GPU-CPU Data (GiB)	GPU-CPU count
40	16416	16	166.90	115.75	45	21.62	1264	24.55	2944	46
40	16448	32	88.80	58.99	45	12.79	636	13.23	1568	49
40	16512	64	47.71	29.64	45	7.73	351	7.14	848	53
40	16640	128	27.30	14.99	45	5.27	191	3.83	456	57
40	16896	256	16.59	8.06	45	3.46	103	2.05	244	61
40	17408	512	11.90	4.57	45	2.61	55	1.09	130	65